



HAL
open science

A Robust Ultra-microporous Cationic Aluminiumbased Metal-Organic Framework with a Flexible Tetra-carboxylate Linker

Shyamapada Nandi, Asma Mansouri, Iurii Dovgaliuk, Philippe Boullay, Gilles Patriarche, Ieuan Cornu, Pierre Florian, Georges Mouchaham, Christian Serre

► **To cite this version:**

Shyamapada Nandi, Asma Mansouri, Iurii Dovgaliuk, Philippe Boullay, Gilles Patriarche, et al.. A Robust Ultra-microporous Cationic Aluminiumbased Metal-Organic Framework with a Flexible Tetra-carboxylate Linker. *Communications Chemistry*, 2023, 6 (1), pp.144. 10.1038/s42004-023-00938-x . hal-04303606

HAL Id: hal-04303606

<https://hal.science/hal-04303606>

Submitted on 23 Nov 2023

HAL is a multi-disciplinary open access archive for the deposit and dissemination of scientific research documents, whether they are published or not. The documents may come from teaching and research institutions in France or abroad, or from public or private research centers.

L'archive ouverte pluridisciplinaire **HAL**, est destinée au dépôt et à la diffusion de documents scientifiques de niveau recherche, publiés ou non, émanant des établissements d'enseignement et de recherche français ou étrangers, des laboratoires publics ou privés.

1 A Robust Ultra-microporous Cationic Aluminium-
2 based Metal-Organic Framework with a Flexible
3 Tetra-carboxylate Linker

4 *Shyamapada Nandi,^{1,2} Asma Mansouri,¹ Iurii Dovgaliuk,¹ Philippe Boullay,³ Gilles Patriarche⁴*
5 *Ieuan Cornu,⁵ Pierre Florian,⁵ Georges Mouchaham,^{1*} and Christian Serre^{1*}*

6 ¹ Institut des Matériaux Poreux de Paris, Ecole Normale Supérieure, ESPCI Paris, CNRS, PSL
7 University 75005 Paris, France.

8 ² Chemistry Division, School of Advanced Sciences, Vellore Institute of Technology, 600127,
9 Chennai, India.

10 ³ Normandie Université, ENSICAEN, UNICAEN, CNRS, CRISMAT, 14050 Caen, France.

11 ⁴ Université Paris-Saclay, CNRS, Centre de Nanosciences et de Nanotechnologies, 91120
12 Palaiseau, France.

13 ⁵ Centre National de la Recherche Scientifique (CNRS), UPR3079 CEMHTI, Université
14 d'Orléans, 1D Av. Recherche Scientifique, CEDEX 2, 45071 Orléans, France.

15 Emails : georges.mouchaham@ens.psl.eu ; christian.serre@ens.psl.eu

16

17 **KEYWORDS:** Metal-Organic Framework, Cationic MOF, Three-dimensional electron
18 diffraction, Hydrolytically Stable, Environment-friendly Synthesis, CO₂ Capture.

19 **ABSTRACT:** Al-based cationic metal-organic frameworks (MOFs) are uncommon. Here, we
20 report a cationic Al-MOF, MIP-213(Al) ([Al₁₈(μ₂-OH)₂₄(OH₂)₁₂(mdip)₆]6Cl·6H₂O) constructed
21 from flexible tetra-carboxylate ligand (5,5'-Methylenediisophthalic acid; H₄mdip). Its crystal
22 structure was determined by the combination of three-dimensional electron diffraction (3DED)
23 and high-resolution powder X-ray diffraction. The structure is built from infinite corner-sharing
24 chains of AlO₄(OH)₂ and AlO₂(OH)₃(H₂O) octahedra forming an 18-membered rings honeycomb
25 lattice, similar to that of MIL-96(Al), a scarce Al-polycarboxylate defective MOF. Despite sharing
26 these structural similarities, MIP-213(Al), unlike MIL-96(Al), lacks the isolated μ₃-oxo-bridged
27 Al-clusters. This leads to an ordered defective cationic framework whose charge is balanced by
28 Cl⁻ sandwiched between two Al-trimers at the corner of the honeycomb, showing strong interaction
29 with terminal H₂O coordinated to the Al-trimers. The overall structure is endowed by a narrow
30 quasi-1D channel of dimension ~4.7 Å. The Cl⁻ in the framework restrains the accessibility of the
31 channels, while the MOF selectively adsorbs CO₂ over nitrogen and possesses high hydrolytic
32 stability.

33 **Introduction.**

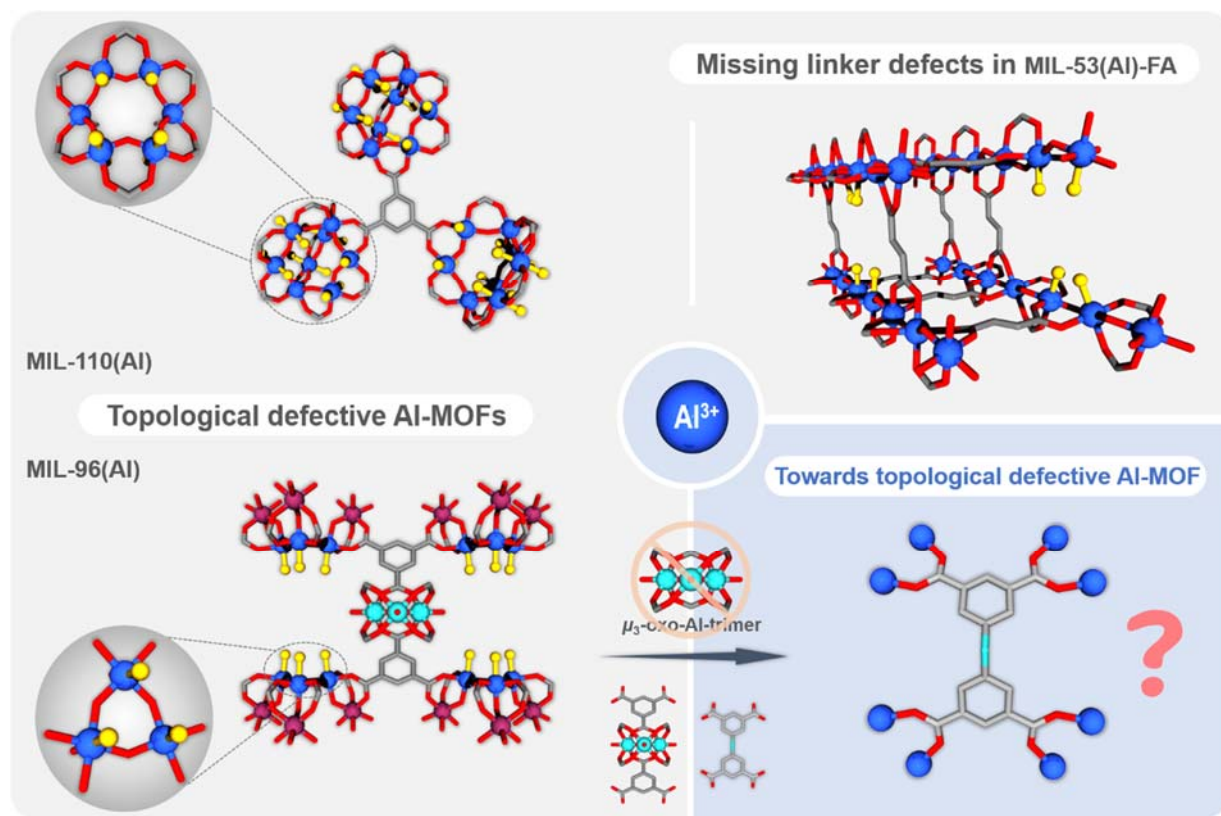
34 Metal-Organic frameworks (MOFs) constructed from inorganic nodes (metal ions,
35 clusters, chains, layers, etc.) linked via organic linkers have emerged as a new class of porous
36 solids. Owing to their ordered porous structure, highly tunable pore size, shape and composition,
37 they have been proposed for a wide range of potential applications such as separation,¹⁻⁸ gas
38 storage,⁹⁻¹⁰ catalysis,¹¹⁻¹³ heat reallocation,¹⁴⁻¹⁵ water harvesting,¹⁶ biomedicine¹⁷⁻¹⁸ etc. Among

39 different classes of MOFs reported so far, trivalent (Al, Cr, Fe) and tetravalent (Ti, Zr, Hf, Ce)
40 metal polycarboxylate MOFs are considered as the most promising candidates due to their high
41 hydrolytic stability compared to different divalent metal carboxylate MOFs.¹⁹⁻²³

42 Defects in MOFs, that break the systematic arrangements of the atoms or motifs within the
43 crystal of the parent framework, has become an important additional tool for tuning their
44 properties. These are mainly related to the organic moieties but can also concern the inorganic
45 building units. In the case of ligand defects, one can distinguish (i) topological defects where
46 usually no bridging ligands are expected as per the topological requirement; and (ii) missing
47 linkers where normally a topologically needed ligand is absent in the structure. In both cases, the
48 absence of bridging ligand can be compensated by the coordination of solvents, modulators or
49 other labile ligands. Thus, both the defects create some potential coordination vacancies around
50 the adjacent metal/clusters and thereby drastically change the properties of the solids. Very
51 recently, defective MOFs have attracted tremendous attention due to their unique properties
52 compared to the non-defective MOFs.²⁴⁻²⁶ Via engineering the defects, and hence the potentially
53 uncoordinated sites, one can provide novel opportunities in adsorption,^{26, 27} catalysis,²⁸ optical,²⁹
54 magnetic,²⁹ and conducting properties,²⁷ etc. Indeed, defect engineered M^{IV}-MOFs enabled
55 enhanced properties compared to the respective non-defective analogues, such as in catalysis,
56 ^{30,31,32} pollutant or organic dye removal, ^{33, 34} heat allocation, ³⁵ and adsorption ^{26, 27, 36, 37}. More
57 importantly, ligand defect has a significant impact on Lewis and Bronsted acidities³⁸ of the solids
58 giving rise to unique binding/active and/or molecular imprinted sites.²⁸ The proton conductivity of
59 the MOFs could also be tuned eventually boosted via grafting of acidic species to the defect sites.³⁹
60 ⁴⁰ It is quite common to observe defects in case of a tetravalent metal-based MOFs such as
61 Zr/Hf/Ce based MOFs. Although these defective MOFs, particularly the Zr-based ones, show very

62 promising properties, controlling the defects onto the SBUs is not a trivial task especially when
63 synthesized in large scale in the presence of a modulator. Similar to Zr/Hf based MOFs, very few
64 Ti based defective MOFs could also be observed.^{41,42} When it turns to the case of trivalent metals-
65 based MOFs such as those based on Fe^{III}, several defective Fe-MOFs has been observed
66 particularly when the MOFs are derived from the Fe-based trimeric oxo/hydroxo clusters.^{43, 44}
67 Interestingly, in the case of Al-MOFs, there exist only very few examples of defective MOFs.⁴⁵
68 The reason for this is that the chemistry of Al MOFs can be quite complex to control leading often
69 to different polymorphs. Besides, in most of the cases, the structures are built from Al-hydroxo
70 chains where it is more challenging to introduce defects (Fig. 1). In contrast, the latter are, in
71 general, more frequently observed in the case of oxo/hydroxo-cluster-based MOFs, although very
72 scarce in the case of Al-MOFs. For instance, Al-trimesates such as MIL-96(Al) and MIL-110(Al)
73 exhibit topological defects leading to the presence of terminal hydroxyl groups and water
74 molecules.^{46,47} Indeed, MIL-96(Al) comprises oxo-centered Al-trimers that are coordinated to
75 bridging trimesates, as well as another 18-member 2D hexagonal secondary building unit made
76 from infinite chains of AlO₄(OH)₂ and AlO₂(OH)₄ octahedra (arranged in a trimeric fashion). The
77 structure contains terminals water molecules as well as terminal hydroxyl groups which potentially
78 act as open metal sites (OMS) or coordinatively unsaturated sites, that might be also used as
79 grafting sites for active metal ions or nanoparticles. These hydroxyls groups could also be replaced
80 by other anions (such as chloride, fluoride, nitrate or acetate depending on the reactants used in
81 the synthesis) as well. Despite such a possibility, it has not been exploited except in the case of
82 fluoride.⁴⁸ Due to its highly functional active sites (terminal water and OH groups), this MOF has
83 been explored for several applications such as CO₂ capture,^{49, 50} catalytic dye degradation,⁵¹ liquid
84 phase absorption of *p*-hydroxybenzoic acid,⁵¹ fluoride removal from water⁴⁸, etc. Series of Al-

85 MOFs derived from di/tri/tetra-carboxylate linkers have been reported to date. However, reports
86 on Al-polycarboxylate MOFs to be either cationic and/or defective remain still extremely rare.^{46,47}
87 For example, the typical dicarboxylates such as terephthalate (1,4-BDC),⁵² isophthalate (1,3-
88 BDC),⁵³ fumarate (FA)⁵⁴ and their derivatives led to rigid or flexible frameworks without any
89 topological defect. Only missing linker defects have been reported such as in the case of MIL-53-
90 FA associated with the presence of Lewis acid sites.⁵⁴ In case of tricarboxylates, although few
91 trimesate MOFs exhibited structural defects, the use of benzene-1, 3, 5-tribenzoate (BTB)⁵⁵ does
92 not lead to any structural defect. Similarly, different tetra carboxylates such as 1,2,4,5 benzene
93 tetracarboxylate (BTcC),^{56, 57} 1,2,4,5-tetrakis-(4-carboxylatophenyl)-benzene (TCPB),⁵⁸
94 tetrakis(4-carboxyphenyl) porphyrin (TCPP),⁵⁹ 1,3,6,8-tetrakis (*p*-benzoic acid) pyrene
95 (TBAPy),⁵⁹ biphenyl tetra carboxylate (BPTC),⁶⁰ led only to rigid or flexible framework without
96 any topological defect. In most cases, one can conclude that when the use of rigid linkers is
97 considered, one ends up with rigid/flexible MOFs without any topological defects, albeit scarce
98 exceptions. Therefore, the idea here was to explore the use of flexible linker for the construction
99 of topologically defective Al-MOFs inspired by MIL-96(Al) structure.



100

101 **Fig. 1: Al-defective MOFs.** Examples of Al-MOFs showing topological defects and missing
 102 linkers as well as our new proposed synthesis strategy to generate a topologically defective MOF
 103 inspired by MIL-96(Al) structure.

104 In this regard, herein we investigated the flexible tetracarboxylic acid linker (5, 5'-
 105 Methylene-diisophthalic acid; H_4mdip ; Supplementary Fig. 1) for the construction of new Al-
 106 MOFs. After screening a wide range of synthesis conditions (solvent, pH, temperature, metal
 107 sources, etc.), we finally obtained a new ultra-microporous MOF having a general formula
 108 $[\text{Al}_{18}(\mu_2\text{-OH})_{24}(\text{OH}_2)_{12}(\text{mdip})_6]6\text{Cl}\cdot 6\text{H}_2\text{O}$ denominated as MIP-213(Al), cationic in nature (MIP
 109 stands for Materials from Institute of Porous Materials of Paris). Its crystalline structure was
 110 determined using a combination of three-dimensional electron diffraction (3DED) and high-
 111 resolution Powder X-ray diffraction (HRPXRD). The MOF exhibits a hexagonal structure very

112 similar to MIL-96(Al) framework as a consequence of similar inorganic secondary building unit
113 (SBU) built from the infinite chains of $\text{AlO}_4(\text{OH})_2$ and $\text{AlO}_2(\text{OH})_3(\text{H}_2\text{O})$ octahedra forming a
114 honeycomb lattice based on 18-membered rings, without, however, the isolated oxo-centered Al-
115 trimers in the case of MIP-213(Al). Consequently, MIP-213(Al) possesses chloride ions which are
116 sandwiched between two topologically defective Al-trimers present at the corner of the
117 honeycomb. Due to the presence of these anions, the pores along [1 0 0] become inaccessible for
118 nitrogen at 77K. To assess the potential of this MOF for adsorption of small gas molecules, and as
119 this compound possesses very high hydrolytic stability of interest for real applications, we have
120 explored the selective adsorption of CO_2 over N_2 at room temperature, taking into account the
121 promises of MIL-96(Al) for the CO_2 capture.⁴⁵

122

123 **Results and Discussion.**

124 MIP-213(Al) was synthesized under ambient pressure conditions employing green
125 solvents. In a typical synthesis, H₄mdip linker was dissolved in equivalent amount of 2M NaOH
126 and added to $\text{AlCl}_3 \cdot 6\text{H}_2\text{O}$ dispersed in a mixture of benzyl alcohol which was preheated to 180°C.
127 The mixture was then refluxed at 200°C overnight. After cooling the mixture to room temperature,
128 the solid off-white powder was isolated via filtration followed by washing with water, ethanol and
129 drying the sample at 80°C. The dried solid product was characterized using PXRD,
130 thermogravimetric analysis (TGA), FTIR and other advanced characterization methods
131 (Supplementary Figs. 2-7).

132 **Structural Characterization and Analysis**

133 Because of the small size of the obtained crystallites (ca.100-300 nm, Supplementary Figs.
134 8-9), we have first attempted to solve the structure from HRPXRD methods. The indexing of the
135 HRPXRD pattern revealed that the material crystallizes in a hexagonal crystal system with space
136 group $P6_3/mmc$ ($N^\circ 194$). However, our initial crystal structure determination from the HRPXRD
137 data was not successful. In addition, our attempts to grow single crystals yielded above the
138 submicronic scale, even under solvothermal conditions, were not successful (Supplementary Figs.
139 8-9), ruling out the structure determination from single crystal X-ray diffraction even under a
140 microfocus synchrotron source. We then considered the assistance of single crystal electron
141 diffraction technique known as 3DED^{61, 62} which allows obtaining structure solution from tiny
142 crystals. The continuous rotation electron diffraction (cRED)⁶³ data has been collected using the
143 instrumental conditions detailed in supporting information (Section: material and methods). The
144 temperature of the sample in the TEM was decreased to 95 K using a cryo-transfer holder, to
145 enhance the stability of the MOF under the electron beam. Two datasets (collected in less than 20
146 seconds) were selected to be merged into a single dataset with an improved combination of
147 resolution and completeness.

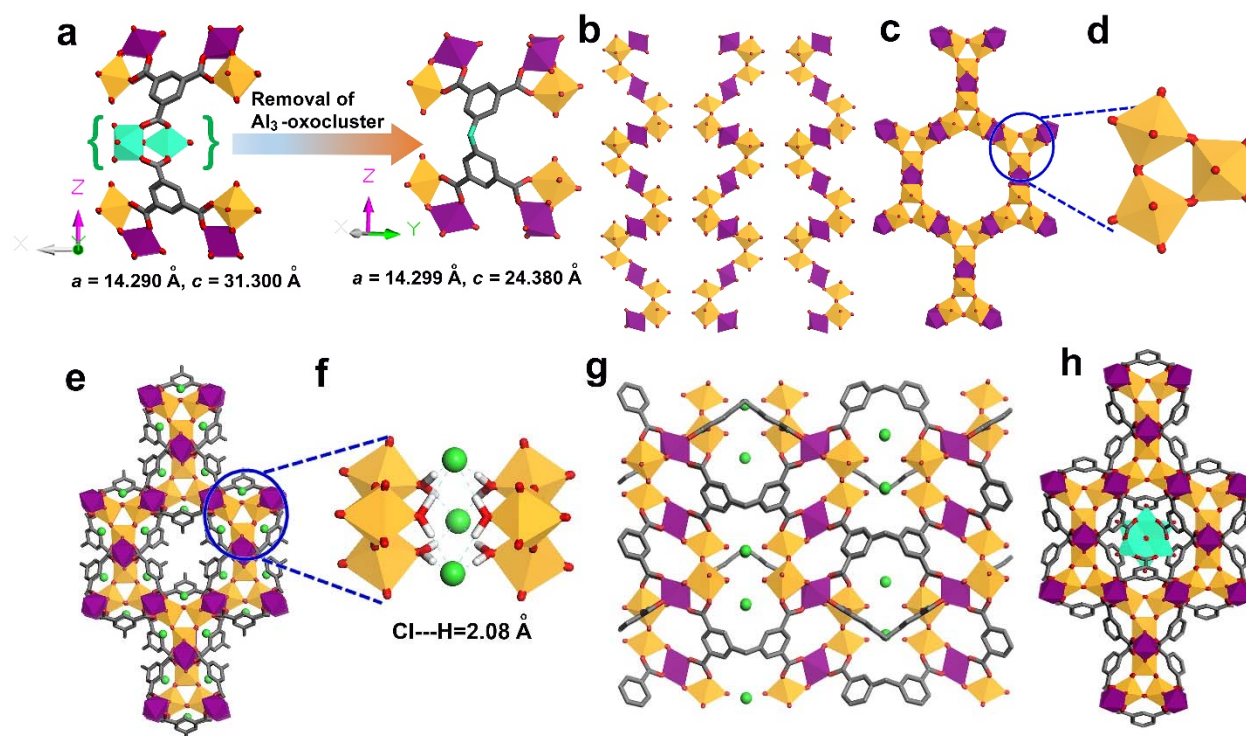
148 The structure solution step gives a 3D density map with well-identified positions for all
149 non-hydrogen atoms (Supplementary Fig. 11). Actually, only a strong residual density present in
150 the voids of the structure seemed to us more difficult to attribute with certainty and was initially
151 thought to be free water molecules. Nonetheless, the presence of water molecules did not match
152 with the observation made from the TGA data (Supplementary Fig. 6) and, therefore, we had to
153 consider other possibilities for the inclusion of solvent molecules to the voids of this framework.
154 STEM imaging of the MOF's particles combined with EDX spectroscopy provides a map of the
155 elemental distribution and indicates the presence of chloride ions homogeneously in the sample

156 (Supplementary Fig. 11). The presence of this halide arises from the salt AlCl_3 used as a precursor
157 for the MOF synthesis. From the initial density map obtained from 3DED data after the structure
158 solution step (Supplementary Fig. 11a), replacing water molecules with Cl^- ions is in good
159 agreement with the highest residual intensity (Supplementary Fig. 12). While the 3DED data were
160 of good quality to provide a structural model, the kinematical refinement convergences to high R
161 factors ($R(\text{obs}) = 33.25\%$, $wR(\text{obs}) = 33.15$) which prevented from any finer structural analysis.
162 The obtained model was thus confirmed using a Rietveld refinement against the laboratory
163 HRPXRD data (Supplementary Fig. 12 and Supplementary Data 1), where satisfying R factors
164 were obtained ($R_{\text{Bragg}} = 13.1\%$, $R_{\text{F}} = 9.01\%$). The inclusion of the Cl^- to the voids of the framework
165 resulted in a better match between the experimental and calculated diffraction patterns compared
166 to inclusion of water molecules.

167 The crystal structure of MIP-213(Al) ($P6_3/mmc$ with $a = 14.2995(3)$ Å) shows strong
168 similarities with the structure of MIL-96(Al) ($P6_3/mmc$ with $a = 14.290$ Å). Only, the c parameters
169 of both crystal structures differ ($31.300(6)$ versus $24.3801(10)$ Å for MIL-96(Al) and MIP-
170 213(Al), respectively) in agreement with the change of the framework connectivity along $[0\ 0\ 1]$.
171 From the geometrical considerations, the exclusion of the μ_3 -oxo-centered isolated Al-trimers from
172 the structure of MIL-96(Al) and the “merging” of its two isophthalate linkers along $[0\ 0\ 1]$ into one
173 5,5'-methylenediisophthalate are, as expected by replacing trimesate by mdip^{4-} linker, at the origin
174 of the framework model of MIP-213(Al) (Fig. 2a).

175 The crystal structure analysis reveals that this MOF is built from the infinite chains of
176 $\text{AlO}_4(\text{OH})_2$ and $\text{AlO}_2(\text{OH})_3(\text{H}_2\text{O})$ octahedra forming a honeycomb lattice based on 18-membered
177 rings which is very similar to the SBU present in MIL-96(Al) (Fig. 2). These SBU layers get
178 connected by the tetracarboxylate linkers (mdip^{4-}) and thereby generate the three-dimensional

179 framework (Fig. 2e). The 3D framework consists of narrow hexagonal channels of dimension ~ 4.7
 180 \AA along $[0\ 0\ 1]$ (Fig. 2e), which are interconnected with another narrow channels present along $[1$
 181 $0\ 0]$.

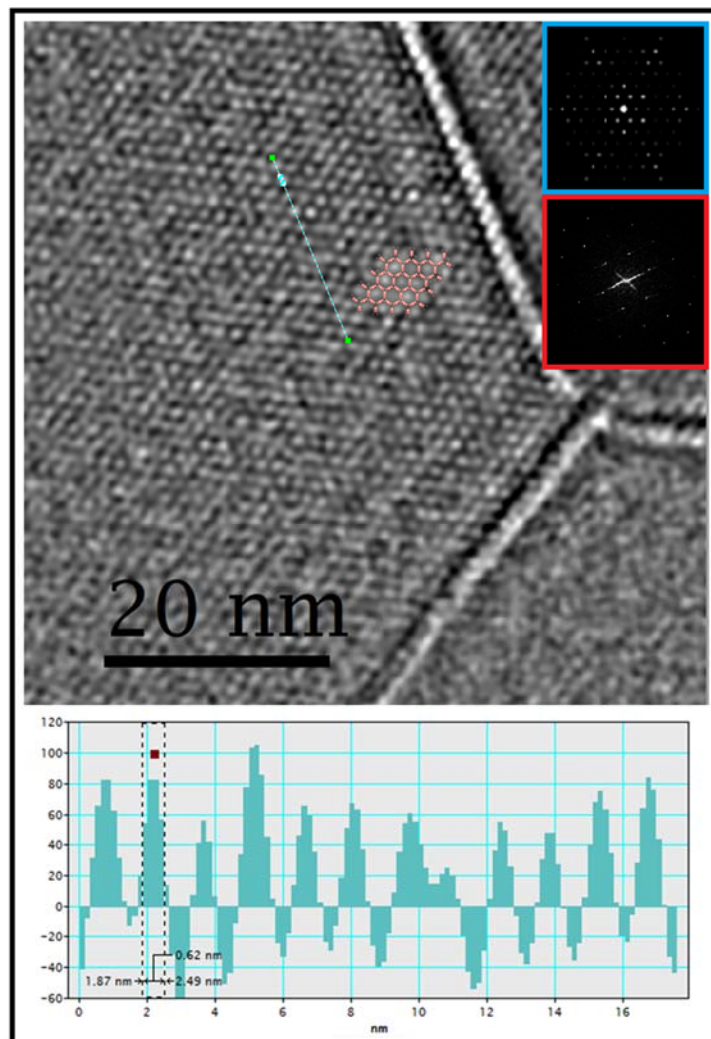


182

183 **Fig. 2: Depiction of the crystal structure of MIP-213(Al) and the structural similarities with**
 184 **MIL-96(Al).** (a) The geometrical similarities of the framework structures of MIL-96(Al) and MIP-
 185 213(Al). (b) Secondary building unit, the infinite chains of $\text{AlO}_4(\text{OH})_2$ and $\text{AlO}_2(\text{OH})_3(\text{H}_2\text{O})$
 186 octahedra present in MIP-213(Al). (c) Inorganic SBU along $[0\ 0\ 1]$ showing the infinite chains of
 187 $\text{AlO}_4(\text{OH})_2$ and $\text{AlO}_2(\text{OH})_3(\text{H}_2\text{O})$ octahedra forming an 18-membered hexagonal honeycomb
 188 layer. (d) Al-trimers present in the corner of the hexagonal honeycomb layers. (e) 3D view of the
 189 crystal structure of MIP-213(Al) along $[0\ 0\ 1]$, showing the narrow corrugated hexagonal channel.
 190 (f) Zoom-in view at the corners of the hexagonal honeycomb showing the exact position of the
 191 chloride ions with typical $\text{Cl}\dots\text{H}$ interaction. (g) 3D view of the crystal structure along $[1\ 0\ 0]$. (h)

192 3D view of the crystal structure of MIL-96(Al) along [0 0 1]. Color code: $\text{AlO}_4(\text{OH})_2$ polyhedra,
193 $\text{AlO}_2(\text{OH})_3(\text{H}_2\text{O})$ polyhedra, carbon, oxygen and chloride atoms are in purple, orange, grey, red,
194 and light-green, respectively (μ_3 -oxo-centered Al-trimers presented by the cyan polyhedral;
195 hydrogen atoms are omitted for clarity).

196 According to the crystallographic structure, this framework shall be positively charged.
197 The extra positive charge of the framework is here balanced by the presence of chloride counter
198 ions which are typically positioned between two Al-trimers present at the corner of the honeycomb
199 as presented in Fig. 2e and 2f. Interestingly, these chloride ions are having strong interaction with
200 the terminal water molecules connected to the Al centers of the Al-trimers with a typical Cl...H
201 distance of ~ 2.08 Å (Fig. 2f). Due to the presence of the chloride ions the channels/cages along [1
202 0 0] become very restricted for gas molecules to enter the channel (Fig. 2g), although such ultra-
203 microporous windows might, as shown previously in the case of MFU-4 for instance, be accessible
204 under specific conditions.⁶⁴ However, the hexagonal channels along the [0 0 1] are quite accessible
205 to the gas molecules. Furthermore, the presence of channels of hexagonal symmetry was directly
206 observed in real space using low-dose HRTEM imaging, from which the unit cell parameters
207 (Supplementary Table 3) and the diameters of the channel are extracted, and the values
208 corroborated well with those from the initial structural model from 3DED data (Fig. 3). The
209 diameter of the channels calculated from the profile line is around 0.6 nm. The full width at half
210 maximum (FWHM) of each peak is defined as the diameter of the corresponding channel (bright
211 spot in the image; Fig. 3).



212
 213 **Fig. 3: Low dose HRTEM image of MIP-213(Al).** Filtered HRTEM image of MIL-213(Al)
 214 oriented along the [0 0 1] axis. The structural model exhibiting the hexagonal channels along the
 215 *c* axis is superposed on the image. The insets are the FFT (red), the simulated electron diffraction
 216 pattern (blue), generated from the ED model using the Crystdiff software.⁶⁵

217
 218 A comparative structural analysis shows very high topological similarities between the MIP-
 219 213(Al) and MIL-96(Al) (Fig. 2h and Supplementary Fig. 13). Both frameworks are built from the
 220 same 18-member hexagonal honeycomb layers from the infinite chains of $\text{AlO}_4(\text{OH})_2$ and
 221 $\text{AlO}_2(\text{OH})_3(\text{H}_2\text{O})/\text{AlO}_2(\text{OH})_4$ octahedra (Supplementary Fig. 13). The main difference between
 222 MIL-96(Al) and MIP-213(Al) is the absence of the μ_3 -oxo-centered isolated Al-trimers in the later

223 one. In the case of MIL-96(Al), if one removes the carboxylate groups connected to the isolated
224 oxo-centered Al-trimers leading to an isophthalate, that accounts to one-half of the mdip⁴⁺ linker,
225 then the generated SBU layer is the same as the SBU layer present in MIP-213(Al) (Supplementary
226 Fig. 13a-13d). Subsequently, in the case of the MIL-96(Al), these SBU layers are connected to
227 each other via the third arm of the trimesate linker connecting the isolated Al-trimers
228 (Supplementary Fig. 13g) whereas in the case of MIP-213(Al) the SBU layers are connected via
229 the methylene carbon of the mdip⁴⁺ linker thereby generating the 3D framework (Supplementary
230 Fig. 13h). The SBU layers are separated by a larger distance (O...O distance between the layers =
231 6.57 Å) compared to that observed in the case of MIP-213(Al) (O...O distance between the layers
232 = 3.20 Å) (Supplementary Fig. 13). Another important difference is that MIL-96(Al) is neutral and
233 contains terminal water/hydroxy ligands which are connected to the Al centers of the Al-trimers
234 present at the corner of the hexagonal honeycomb layer. In MIP-213(Al) the framework exhibits
235 a positive charge that is balanced by the chloride ions present in between the Al-trimers from two
236 different layers (Supplementary Fig. 13j and 1e, 1f) while all the oxygen atoms connected to the
237 Al-trimers at the corner of the hexagonal honeycomb are from the water molecules. Thus MIP-
238 213(Al) possesses a hexagonal corrugated narrow channel along [0 0 1]. Nevertheless, in case of
239 MIL-96(Al) this hexagonal channel is blocked by the isolated μ_3 -oxo centered Al-trimers
240 (Supplementary Fig. 13i). Despite being cationic in nature, this framework is highly thermally
241 stable under oxygen atmosphere as observed from the variable temperature PXRD and TGA
242 measurement (Supplementary Figs. 5-6). This can be supported by the fact that the chloride
243 counter ions do not easily leave the structure due to a strong interaction with the terminal water
244 molecules. Overall, although the structures of MIP-213 and MIL-96 are obtained from 2 different
245 ligands (pure organic for the former, and metalo-ligand for the latter), they are structurally quite

246 well related thanks to the 18-membered hexagonal honeycomb layer SBU at the origin of both
247 MOFs, with specific chemical features for each.

248 **Solid State NMR Studies**

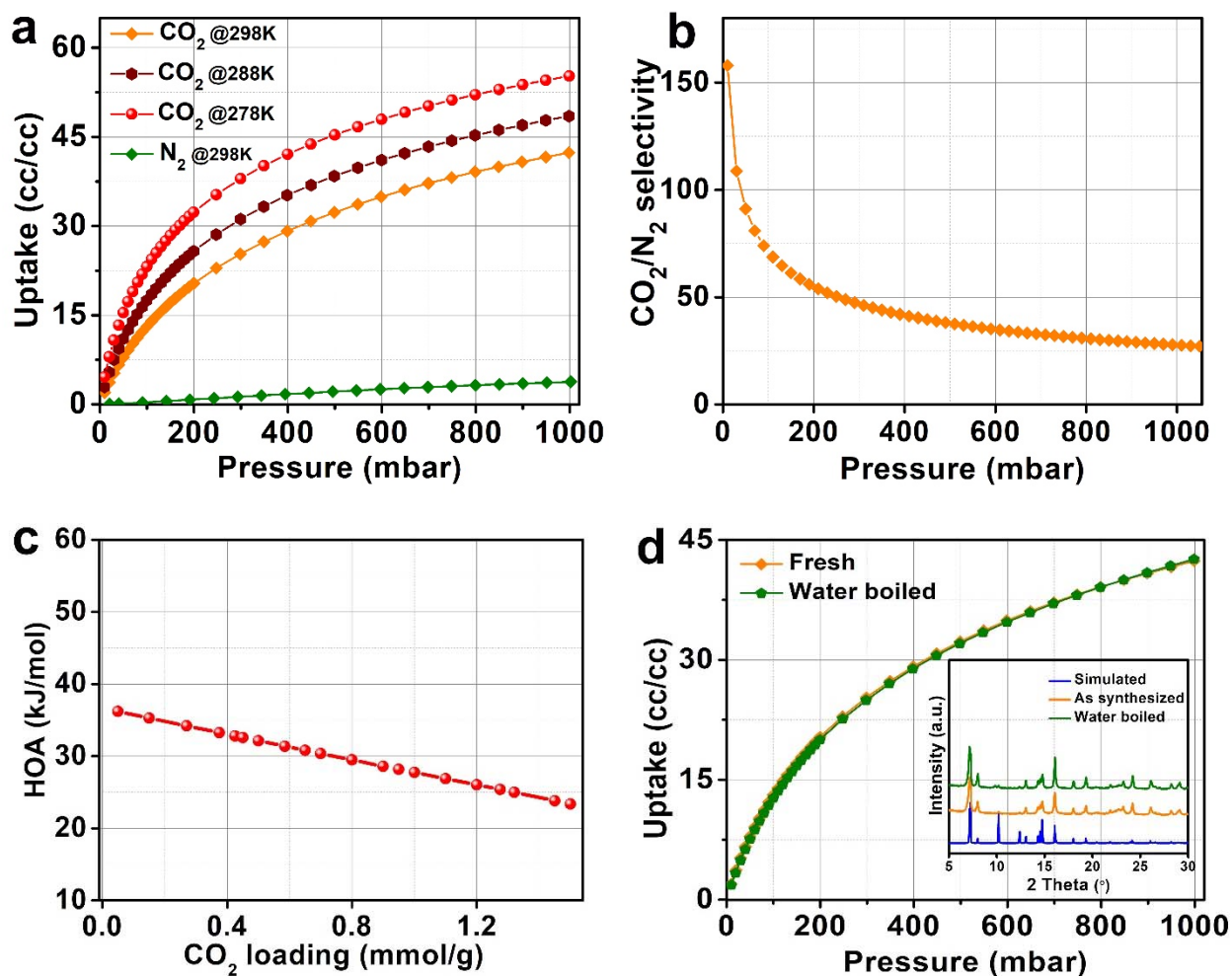
249 Furthermore, for a deeper structural understanding solid state NMR has been considered
250 with ^1H and ^{13}C NMR to provide information on the linker's structure whereas ^{27}Al NMR is
251 expected to shed light on the metal ions configurations. Supplementary figure 14 shows the $^1\text{H}/^{13}\text{C}$
252 two-dimensional correlation spectra evidencing the various proton and carbon environment and
253 their connectivity. On the carbon side, intensities found around 130 ppm are assigned to the
254 aromatic carbons (C4, C5, C14, C15) while some additional resonances found around 170 ppm
255 and 40 ppm correspond to the carboxylates (C3) and methylene bridge (C17) carbons, respectively.
256 To confirm this assignment, first principle calculations of NMR parameters were performed on the
257 structure with proton positions optimized. The results are given in Supplementary Table 4 and
258 show very reasonable agreement with the experimental spectrum (Supplementary Fig. 15).
259 Additional resonances observed around 120 ppm and 60 ppm belongs to residual solvents (benzyl
260 alcohol). Non-protonated carbons C3, C5 and C14 are further evidenced by their marked
261 dependence to the contact time in the CPMAS experiments (Supplementary Fig. 16). This provides
262 the full assignment of the six inequivalent carbons as shown in Supplementary Table 4. On the
263 proton side, the 2D HETCOR along with the DFT calculations allows us to propose the assignment
264 of the six inequivalent protons as shown in supplementary Fig. 17. The ^1H signals absent from the
265 ^1H HETCOR projection correspond to the non-carbonated protons $\mu_2\text{-OH}$ (H13 and H19) and
266 structural H_2O (H7), which are found, respectively, at around 2 ppm and 7 ppm, (Supplementary
267 Fig. 18) in good agreement with the DFT calculation (Supplementary Table 4). An additional
268 resonance is needed around 5 ppm and assigned to residual benzyl alcohol as it correlates in the

269 $^{13}\text{C}\{^1\text{H}\}$ HETCOR to the carbon site assigned above to this residual solvent. Overall, the full
270 assignment of the ^{13}C and ^1H spectra confirm the structural model of the linkers derived in the
271 preceding sections. The ^{27}Al spectra shown a complex lineshape resulting from overlapping sites
272 partially resolved in an MQMAS experiments (Supplementary Figs. 19-20), showing 3
273 components with distribution of NMR parameters and, hence, distribution of structural
274 environments. This 2D experiment can be satisfactorily simulated with 1 site presenting a strong
275 quadrupolar coupling constant ($C_Q \sim 7.3$ MHz) and 2 with rather small ones ($C_Q \sim 2.5$ MHz). The
276 crystal structure predicts only two inequivalent aluminum sites (Al8 and Al9) and the DFT
277 calculation shows that they possess contrasted C_Q s: $C_Q(\text{Al8}) = 8.65$ MHz and $C_Q(\text{Al9}) = 1.24$ MHz,
278 allowing to assign the site with $C_Q \sim 7.3$ MHz to Al8 of the form $\text{Al}(\text{OAl})_2(\text{OC})_4$. For the Al9 site
279 of the form $\text{Al}(\text{OAl})_3(\text{OC})_2(\text{H}_2\text{O})$, we expect a smaller C_Q , but two sharp resonances are observed
280 experimentally. A double-quantum 2Q-filtered experiment (Supplementary Fig. 21) which selects
281 aluminum with close-by proximities, does remove the sharp line in the middle of the spectrum,
282 this one being therefore attributed to an isolated aluminum arising from an impurity. The full
283 2Q/1Q experiment also evidences Al9/Al9 and Al9/Al8 proximities, and absence of Al8/Al8
284 proximities, in full agreement with the crystal structure. This allows an attribution of the two
285 resonances corresponding to the two inequivalent aluminum sites expected from the
286 aforementioned structure and confirms the validity of the structure derived above.

287 **Gas Sorption Analysis**

288 As established from the structural investigation, the material possesses microporous
289 channels. The permanent porosity of this MOF was established from the N_2 sorption at 77 K
290 (Supplementary Fig. 22). The material does not adsorb much N_2 even at 77 K (saturation uptake
291 ~ 1.0 mmol g^{-1}) with a calculated BET surface area of 60 m^2g^{-1} , which is much lower compared to

292 the one of MIL-96(Al) ($>600 \text{ m}^2\text{g}^{-1}$). This can be explained in the case of MIP-213(Al), by the fact
293 that the channels along [1 0 0] are inaccessible to N_2 due to the presence of the chloride ions right
294 at the center of the channels (details on ion exchange attempts are available in the Supplementary
295 Information). Although, in case of MIP-213 the channel along the [0 0 1] are open but the small
296 channel diameter restricts the N_2 molecule to diffuse. Considering the ultra-micropores present in
297 MIP-213(Al), we further tested the CO_2 capture properties of this MOF at room temperature (Fig.
298 4 and Supplementary Data 2). Interestingly at 298K the material selectively adsorbs CO_2 over N_2
299 (CO_2 uptake = 17.5 cc/cc at 0.15 bar against 3.8 cc/cc for N_2 at 298K and 1 Bar). Such a lower
300 CO_2 uptake of MIP-213(Al) compared to MIL-96(Al) was expected because of the presence of
301 narrow channels partially occupied by the chloride ions in MIP-213(Al). An IAST prediction from
302 the single component isotherms yielded a CO_2/N_2 selectivity of 60 (Fig. 4b and Supplementary
303 Fig. 23) at 0.15 bar which is quite good in a view of post-combustion carbon capture applications.
304 In fact, the selectivity value is slightly higher than some of the Al, Sc and Zr based microporous
305 MOFs such as MIL-96(Al) (S= 40), ScBDC (S=40), UiO-66(Zr) (S=12), UiO-66(Zr)_BTeC
306 (S=30), UiO-66(Zr)_NH₂ (S=37) but comparable/slightly less than some of the microporous Al/Ti
307 MOFs such as MIL-91(Al) (S=68), MIL-91(Ti) (S=150), MIL-69(Al) (S=120).^{49,66}



308

309 **Fig. 4: CO₂ and N₂ sorption data of MIP-213(Al) showing its selective CO₂ capture**

310 **property and high hydrolytic stability.** (a) CO₂ and N₂ isotherms on MIP-213(Al) collected at

311 different temperatures. (b) CO₂/N₂ selectivity predicted using IAST model employing a nominal

312 composition of 15CO₂:85N₂. (c) HOA plot derived from a virial calculation employing CO₂

313 isotherm at 3 different temperatures (278, 288 and 298 K). (d) A comparative 298 K CO₂ isotherm

314 of the fresh sample and water boiled sample showing the hydrolytic stability of the MOF. The inset

315 shows the PXRD patterns (Cu K α radiation, $\lambda = 1.5406 \text{ \AA}$) of the fresh and water boiled sample.

316 Furthermore, a virial analysis of the CO₂ isotherms at 273, 283 and 298 K yielded a zero coverage

317 heat of adsorption (HOA) of 37 kJmol⁻¹ (Fig. 4c and Supplementary Fig. 24). The water sorption

318 isotherm at 298 K shows a clear type I isotherm indicating very strong interactions between the
319 water molecules and the framework at low pressure (Supplementary Fig. 25). This is in good
320 agreement with the structural model. One of the most important properties of MOFs to be
321 implemented in any potential industrial applications is the robustness under humid atmosphere or
322 the hydrolytic stability of the MOF.⁶⁷ Considering this we have subjected this MOF for stability
323 tests under boiling water conditions. Interestingly, there was no sign of structural or chemical
324 degradation even after 24 hours of boiling as evidenced from the PXRD data (Fig. 4d) as well as
325 CO₂ adsorption isotherm on the water boiled sample, which further confirms the hydrolytic
326 stability or robustness of this MOF (Fig. 4d).

327 In conclusion, based on a fine structural analysis and a “merging” strategy when replacing
328 tricarboxylate by a flexible tetracarboxylate linker, we have developed a rare example of cationic
329 Al-based MOF with topological defective sites. The structure elucidation from both 3DED and
330 HRPXRD data for this MOF was complemented by low-dose HRTEM imaging and EDX chemical
331 mapping. The MOF is built from the infinite chains of AlO₄(OH)₂ and AlO₂(OH)₄ octahedra which
332 form 18-membered hexagonal honeycomb layers, similar to those present in MIL-96(Al).
333 Although both MOFs share similar SBU, they strongly differ in some other chemical aspects.
334 Unlike MIL-96(Al), MIP-213(Al) does not contain isolated μ_3 -oxo-centered Al-trimers leading to
335 an overall cationic framework, where chloride ions balance the extra positive charge in the
336 framework. Although the presence of these chloride ions in the framework makes this solid less
337 porous (at least to N₂ at 77 K) compared to MIL-96(Al), this MOF still selectively adsorb CO₂
338 over N₂ with a selectivity of 60 at 0.15 bar and 298 K. Moreover, the reported MOF possess high
339 hydrolytic stability and could be applied for many other applications utilizing the
340 defective/cationic nature and/or Lewis acidity. Considering the challenge of developing Al MOFs

341 with controlled defects, this study will pave the way for the design of new Al-based defective
342 MOFs for versatile applications in near future.

343 **Methods.**

344 **Synthesis of MIP-213(Al).**

345 **Milligram-scale synthesis:**

346 MIP-213(Al) was synthesized in a typical ambient pressure reflux synthesis method employing
347 $\text{AlCl}_3 \cdot 6\text{H}_2\text{O}$ and H_4mdip linker, water, benzyl alcohol and NaOH. In a typical synthesis, 0.723g of
348 $\text{AlCl}_3 \cdot 6\text{H}_2\text{O}$ (3 mmol) was dispersed in 18 ml of Benzyl alcohol and the mixture was heated to 180
349 °C. To this a solution of H_4mdip 0.345g (1 mmol) in 2ml of 2M NaOH was added under continuous
350 stirring. Additional 8 ml distilled water was added to the mixture. The reaction mixture was then
351 refluxed at 200 °C for 16 hours. After cooling the reaction to room temperature, the off-white
352 powder was filtered and washed with 20 ml of water and 10 ml of ethanol. The final product was
353 then air dried (yield = 440 mg). The powder product was then characterized using PXRD, IR, TGA
354 and adsorption analysis. The synthesis can be done in a different scale as per the requirement.

355 **Gram-scale synthesis:**

356 In a typical synthesis, 7.23g of $\text{AlCl}_3 \cdot 6\text{H}_2\text{O}$ (30 mmol) was dispersed in 180 ml of Benzyl alcohol
357 and the mixture was heated to 180 °C. To this a solution of H_4mdip 3.45g (10 mmol) in 20ml of
358 2M NaOH was added under continuous stirring. Additional 80 ml distilled water was added to the
359 mixture. The reaction mixture was then refluxed at 200°C for 16 hours. After cooling the reaction
360 to room temperature, the off-white powder was filtered and washed with 100ml of water and 60
361 ml of ethanol. The final product was then air dried (yield = 4.66 g).

362 **Note:** The synthesis temperature could be reduced up to 160 °C but with longer synthesis time (up
363 to 48h).

364 **Characterization of MIP-213(Al).**

365 **The crystal structure determination and refinement from HRPXRD:**

366 The unit cell parameters and the space group of MIP-213(Al) have been indexed using the program
367 EXPO2014.⁶⁸ Although accurate cell parameters and the space group were determined from the
368 indexing of the powder pattern, crystal structure determination was not successful (*See supporting*
369 *information for more details*). The refinement using the Rietveld method was based on the model
370 from 3DED using Fullprof.⁶⁹ The refinement of the powder X-ray diffraction data required the
371 inclusion of benzyl alcohol solvent in the large cavities.

372 **cRED data collection and structure determination:**

373 The cRED data were collected on a JEOL F200 cold-FEG operated at 200 kV, equipped with a
374 GATAN RIO16 camera. A series of 2D electron diffraction patterns are acquired while
375 continuously rotating the crystal using the Digital Micrograph plugin insteadMatic.⁷⁰ The
376 diameter of the parallel beam was set to 300 nm obtained by inserting a 10 μm condenser aperture.
377 The sample was cooled down to a lower temperature (95K) in the TEM using a Gatan ElsaTM cryo-
378 transfer tomography holder, to reduce the electron beam damage.

379 Several cRED datasets were recorded and processed using PETS 2.⁷¹ Two cRED datasets
380 (Supplementary Table 1) collected on isolated crystals were kept to obtain the result presented
381 here. These two datasets were merged in order to obtain a data completeness of 95.3% for a 0.71
382 Å resolution. The structure was solved using SUPERFLIP program (charge flipping method)⁷² and
383 refined using JANA2020⁷³ using electron scattering factors. The density maps (electrostatic
384 potential map in Supplementary Figure 11 and difference Fourier maps in Supplementary Figure
385 12) are visualized using VESTA.⁷⁴ A summary of the data collection and structure refinement are
386 given in Supplementary Table 2.

387 **Low-dose high-resolution transmission electron microscopy:**

388 Low-dose HRTEM data were collected on the FEI Titan 80-300 E-TEM microscope equipped
389 with the Gatan K2 direct-detection electron counting camera (DDEC), operated at 300 kV. An
390 electron dose rate of $8 \text{ e}^- \text{Å}^{-2}$ is used. The “HRTEM filter” was used to apply a Wiener filter,
391 followed by the Average Background Subtraction Filter (ABSF). The details to calculate the
392 channel diameter is provided in the supporting information.

393 **High-resolution scanning transmission microscopy:**

394 High-resolution scanning transmission microscopy images (HRSTEM) were acquired on a FEI
395 Titan Themis microscope 200 corrected for spherical aberrations on the probe, operating at 200
396 kV, equipped with a Ceta 16M hybrid camera from ThermoFischer Scientific capable of working
397 under low-dose conditions.

398 **Solid state NMR:**

399 ^1H , ^{13}C and ^{27}Al spectra were obtained on a Bruker Avance III 17.6 T spectrometer operating at
400 750.0 MHz using magic angle spinning at 30 kHz. Direct spectra were obtained using a Hahn echo
401 sequence with radiofrequency fields. Direct ^{13}C NMR spectra were obtain using a CPMAS
402 experiment. ^{27}Al was obtained using a quantitative pulse at $\nu_{\text{rf}}(^{27}\text{Al}) = 50 \text{ kHz}$, and a recycle delay
403 of 0.3 s based on estimated T1 measurements done by saturation-recovery experiments. 2Q/1Q
404 ^{27}Al - ^{27}Al correlation was used with a $R2_1^2$ recoupling (*A detailed procedure is provided in the*
405 *supporting information*).

406

407 **ASSOCIATED CONTENT**

408 **Data Availability**

409 Supporting information contains all the synthetic and experimental details as well as
410 Supplementary methods (PXRD, N₂, CO₂ and water sorption, TGA, FTIR, etc.) and data. This
411 material is available free of charge from <https://www.nature.com/commschem/> or from the authors
412 on request. The crystallographic structure reported in this study has been deposited at the
413 Cambridge Crystallographic Data Centre (CCDC), under deposition number 2246502. CIF can be
414 obtained free of charge from The Cambridge Crystallographic Data Centre or directly downloaded
415 from the editor webpage as Supplementary Data 1. IAST and related numerical source data are
416 available as Supplementary Data 2.

417 **AUTHOR INFORMATION**

418 **Corresponding Authors**

419 **Georges Mouchaham and Christian Serre**

420 *E-mails: georges.mouchaham@ens.psl.eu, christian.serre@ens.psl.eu

421

422 **Author Contributions**

423 The manuscript was written through the contributions of all authors. All authors have given
424 approval to the final version of the manuscript. SN performed towards the synthesis,
425 characterization and CO₂ capture studies of the material. AM, ID, GP, PB and CS contributed
426 towards the structure solution. IC and PF contributed towards the NMR experiments and analyzed
427 the data. GM and CS supervised the work and contributed towards the overall concept.

428 **Notes**

429 The authors declare no competing interest.

430

431 **ACKNOWLEDGMENT**

432 SN, GM and CS acknowledge the European Union’s Horizon 2020 research and innovation
433 programme under grant agreement No. 831975 (MOF4AIR project) for providing financial
434 support. AM, GM, GP and CS are thankful to the Region Ile-de-France in the framework of DIM
435 RESPORE for the financial support. The authors acknowledge the support from the CNRS-CEA
436 “METSA” French network (FR CNRS 3507) on the platform IRMA (CRISMAT-Caen) and from
437 the Plateform Nanomax (Ecole Polytechnique) for the use of a cutting-edge microscope and
438 camera.

439

440 **REFERENCES**

- 441 (1) Barea, E., Montoro, C., & Navarro, J. A. R. Toxic gas removal – metal–organic frameworks
442 for the capture and degradation of toxic gases and vapours. *Chem. Soc. Rev.*, **43**, 5419-5430
443 (2014).
- 444 (2) Woellner, M. *et al.* Adsorption and Detection of Hazardous Trace Gases by Metal–Organic
445 Frameworks. *Adv. Mater.* **30**, 1704679 (2018).
- 446 (3) Han, X., Yang, S., & Schröder, M. Porous metal–organic frameworks as emerging sorbents
447 for clean air. *Nat. Rev. Chem.* **3**, 108-118 (2019).
- 448 (4) Carter, J. H. *et al.* Exceptional Adsorption and Binding of Sulfur Dioxide in a Robust
449 Zirconium-Based Metal–Organic Framework. *J. Am. Chem. Soc.* **140**, 15564-15567 (2018).
- 450 (5) Tchalala, M. R. *et al.* Fluorinated MOF platform for selective removal and sensing of SO₂ from
451 flue gas and air. *Nat. Commun.* **10**, 1328; 10.1038/s41467-019-09157-2 (2019).

- 452 (6) Zhang, Z., Yao, Z. -Z., Xiang, S. & Chen, B. Perspective of microporous metal–organic
453 frameworks for CO₂ capture and separation. *Energy Environ. Sci.* **7**, 2868-2899 (2014).
- 454 (7) Zhao, X., Wang, Y., Li, D. S., Bu, X. & Feng, P. Metal–Organic Frameworks for Separation.
455 *Adv. Mater.* **30**, 1705189 (2018).
- 456 (8) Kumar, A., *et al.* Direct Air Capture of CO₂ by Physisorbent Materials. *Angew. Chem. Int. Ed.*
457 **54**, 14372-14377 (2015).
- 458 (9) Mason, J. A., Veenstra, M. & Long, J. R. Evaluating metal–organic frameworks for natural
459 gas storage. *Chem. Sci.* **5**, 32-51 (2014).
- 460 (10) Li, B., Wen, H. M., Zhou, W. & Chen, B. Porous Metal–Organic Frameworks for Gas
461 Storage and Separation: What, How, and Why?. *J. Phys. Chem. Lett.* **5**, 3468-3479 (2014).
- 462 (11) Pascanu, V., Miera, G. G., Inge, A. K. & Martín-Matute, B. Metal–Organic Frameworks
463 as Catalysts for Organic Synthesis: A Critical Perspective. *J. Am. Chem. Soc.* **141**, 7223-7234
464 (2019).
- 465 (12) Kornienko, N. *et al.* Metal–Organic Frameworks for Electrocatalytic Reduction of Carbon
466 Dioxide. *J. Am. Chem. Soc.* **137**, 14129-14135 (2015).
- 467 (13) Zheng, F., Zhang, Z., Zhang, C. & Chen, W. Advanced Electrocatalysts Based on
468 Metal–Organic Frameworks. *ACS Omega* **5**, 2495-2502 (2020).
- 469 (14) Lenzen, D. *et al.* A metal-organic framework for efficient water-based ultra-low-
470 temperature-driven cooling. *Nat. Commun.* **10**, 3025; 10.1038/s41467-019-10960-0 (2019).

- 471 (15) Wang, S. *et al.* A robust large-pore zirconium carboxylate metal–organic framework for
472 energy-efficient water-sorption-driven refrigeration. *Nat. Energy* **3**, 985-993; 10.1038/s41560-
473 018-0261-6 (2018).
- 474 (16) Kim, H. *et al.* Water harvesting from air with metal-organic frameworks powered by
475 natural sunlight. *Science*, **356**, 430-434 (2017).
- 476 (17) McKinlay, A. C. *et al.* BioMOFs: Metal–Organic Frameworks for Biological and Medical
477 Applications. *Angew. Chem. Int. Ed.* **49**, 6260-6266 (2010).
- 478 (18) Pinto, R. V. *et al.* Tuning Cellular Biological Functions Through the Controlled Release of
479 NO from a Porous Ti-MOF. *Angew. Chem. Int. Ed.* **59**, 5135-5143 (2020).
- 480 (19) Serre, C. *et al.* Very Large Breathing Effect in the First Nanoporous Chromium (III)-Based
481 Solids: MIL-53 or CrIII(OH)·{O₂C–C₆H₄–CO₂}·{HO₂C–C₆H₄–CO₂H}_x·H₂O_y. *J. Am. Chem.*
482 *Soc.* **124**, 13519-13526 (2002).
- 483 (20) Férey, G. *et al.* A Chromium Terephthalate-Based Solid with Unusually Large Pore
484 Volumes and Surface Area. *Science* **309**, 2040-2042 (2005).
- 485 (21) Abtab, S. M. T. *et al.* Reticular Chemistry in Action: A Hydrolytically Stable MOF
486 Capturing Twice Its Weight in Adsorbed Water. *Chem* **4**, 94-105 (2018).
- 487 (22) Dai, S., Nouar, F., Zhang, S., Tissot, A. & Serre, C. One-Step Room-Temperature
488 Synthesis of Metal (IV) Carboxylate Metal-Organic Frameworks. *Angew. Chem.* **133**, 4328-
489 4334 (2021).

- 490 (23) Mouchaham, G. *et al.* Metal-Organic Frameworks and Water: ‘From Old Enemies to
491 Friends’. *Trends in Chemistry* **2**, 910 (2020).
- 492 (24) Ren, J. *et al.* Structural defects in metal–organic frameworks (MOFs): Formation, detection
493 and control towards practices of interests. *Coord. Chem. Rev.* **349**, 169-197 (2017).
- 494 (25) Sholl, D. S. & Lively, R. P. Defects in Metal-Organic Frameworks: Challenge or
495 Opportunity?. *J. Phys. Chem. Lett.* **6**, 3437-3444 (2015).
- 496 (26) Thornton, A. W., Babarao, R., Jain, A., Trouselet, F. & Coudert, F.-X. Defects in metal-
497 organic frameworks: a compromise between adsorption and stability? *Dalton Trans.* **45**, 4352-
498 4359 (2016).
- 499 (27) Dissegna, S., Epp, K., Heinz, W. R., Kieslich, G. & Fischer, R. A. Defective Metal-Organic
500 Frameworks. *Adv. Mater.* **30**, 1704501 (2018).
- 501 (28) García-Baldoví, A. *et al.* Active site imprinting on Ti oxocluster metal–organic
502 frameworks for photocatalytic hydrogen release from formic acid. *Energy Environ. Sci.* **16**,
503 167-177 (2023).
- 504 (29) Xiang, W., Zhang, Y., Chen, Y., Liu, C. J. & Tu, X. Synthesis, characterization and
505 application of defective metal-organic frameworks: current status and perspectives. *J. Mater.*
506 *Chem. A*, **8**, 21526-21546 (2020).
- 507 (30) Fu, Q. *et al.* Defect-engineered MOF-808 with highly exposed Zr sites as highly efficient
508 catalysts for catalytic transfer hydrogenation of furfural. *Fuel* **327**, 125085 (2022).

- 509 (31) Rimoldi, M. *et al.* Catalytic Zirconium/Hafnium-Based Metal-Organic Frameworks. *ACS*
510 *Catal.* **7**, 997-1014 (2017).
- 511 (32) Liu, X., Hu, C., Wu, J., Cui, P. & Wei, F. Defective NH₂-UiO-66 (Zr) effectively
512 converting CO₂ into cyclic carbonate under ambient pressure, solvent-free and co-catalyst-free
513 conditions. *Chin. J. Chem. Eng.* **43**, 222-229 (2022).
- 514 (33) Yuan, N., Gong, X., Sun, W. & Yu, C. Advanced applications of Zr-based MOFs in the
515 removal of water pollutants. *Chemosphere* **267**, 128863 (2021).
- 516 (34) Liu, B., Liu, M., Xie, Z., Li, Y. & Zhang, A. Performance of defective Zr-MOFs for the
517 adsorption of anionic dyes. *J. Mater. Sci.* **57**, 5438-5455 (2022).
- 518 (35) Cho, K. H. *et al.* Defective Zr-Fumarate MOFs Enable High-Efficiency Adsorption Heat
519 Allocations. *ACS Appl. Mater. Interfaces* **13**, 1723-1734 (2021).
- 520 (36) Yoskamtorn, T. *et al.* Responses of Defect-Rich Zr-Based Metal–Organic Frameworks
521 toward NH₃ Adsorption. *J. Am. Chem. Soc.* **143**, 3205-3218 (2021).
- 522 (37) Lin, S., Zhao, Y. & Yun, Y. S. Highly Effective Removal of Nonsteroidal Anti-
523 inflammatory Pharmaceuticals from Water by Zr(IV)-Based Metal-Organic Framework:
524 Adsorption Performance and Mechanisms. *ACS Appl. Mater. Interfaces*, **10**, 28076-28085
525 (2018).
- 526 (38) Taddei, M. When defects turn into virtues: The curious case of zirconium-based metal-
527 organic frameworks. *Coord. Chem. Rev.* **343**, 1-24 (2017).

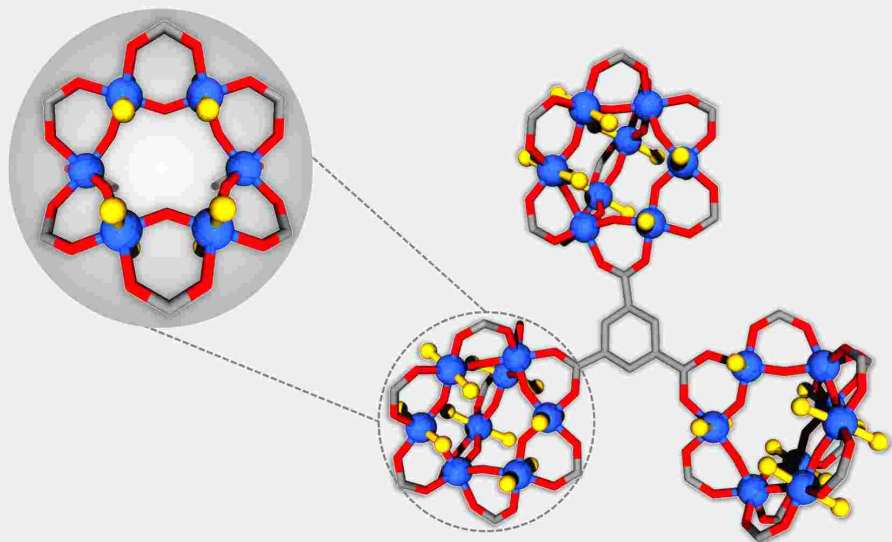
- 528 (39) Chena, X. & Li, G. Proton conductive Zr-based MOFs. *Inorg. Chem. Front.* **7**, 3765-3784
529 (2020).
- 530 (40) Basu, O., Mukhopadhyay, S., Laha, S., Das, S. K. Defect Engineering in a Metal-Organic
531 Framework System to Achieve Super-Protonic Conductivity. *Chem. Mater.* **34**, 6734-6743
532 (2022).
- 533 (41) Wang, S. *et al.* A phase transformable ultrastable titanium-carboxylate framework for
534 photoconduction. *Nat. Commun.* **9**, 1660; 10.1038/s41467-018-04034-w (2018).
- 535 (42) Wang, S. *et al.* Toward a Rational Design of Titanium Metal-Organic Frameworks. *Matter*
536 **2**, 440-450 (2020).
- 537 (43) Duan, T., Jiang, H., Wu, W., Lin, D., Yang, K. Defective iron based metal-organic
538 frameworks derived from zero-valent iron for highly efficient fenton-like catalysis, *J. Hazard.*
539 *Mater.* **445**, 130426 (2023).
- 540 (44) Feng, D. *et al.* Kinetically tuned dimensional augmentation as a versatile synthetic route
541 towards robust metal-organic frameworks. *Nat Commun.* **5**, 5723 (2014).
- 542 (45) Shan, Y., Zhang, G., Shi, Y. & Pang, H. Synthesis and catalytic application of defective
543 MOF materials. *Cell Reports Physical Science* **4**, 101301 (2023)
- 544 (46) Loiseau, T. *et al.* MIL-96, a Porous Aluminum Trimesate 3D Structure Constructed from
545 a Hexagonal Network of 18-Membered Rings and μ_3 -Oxo-Centered Trinuclear Units. *J. Am.*
546 *Chem. Soc.* **128**, 10223-10230 (2006).

- 547 (47) Volkringer, C. *et al.* A microdiffraction set-up for nanoporous metal–organic-framework-
548 type solids. *Nat. Mater.* **6**, 760-764 (2007).
- 549 (48) Wang, X. *et al.* Synthesis and Study of an Efficient Metal-Organic Framework Adsorbent
550 (MIL-96(Al)) for Fluoride Removal from Water. *J. Nanomater.* **2019**, Article ID 3128179;
551 10.1155/2019/3128179 (2019).
- 552 (49) Benoit, V. *et al.* A promising metal–organic framework (MOF), MIL-96(Al), for CO₂
553 separation under humid conditions. *J. Mater. Chem. A* **6**, 2081-2090 (2018).
- 554 (50) Benzaqui, M. *et al.* Revisiting the Aluminum Trimesate-Based MOF (MIL-96): From
555 Structure Determination to the Processing of Mixed Matrix Membranes for CO₂ Capture.
556 *Chem. Mater.* **29**, 10326-10338 (2017).
- 557 (51) Rizwan, M. *et al.* Cascade applications of robust MIL-96 metal organic frameworks in
558 environmental remediation: Proof of concept. *Chem. Eng. J.* **341**, 262-271 (2018).
- 559 (52) Loiseau, T. *et al.* A Rationale for the Large Breathing of the Porous Aluminum
560 Terephthalate (MIL-53) Upon Hydration. *Chem. Eur. J.* **10**, 1373-1382 (2004).
- 561 (53) Reinsch, H. *et al.* Structures, Sorption Characteristics, and Nonlinear Optical Properties of
562 a New Series of Highly Stable Aluminum MOFs. *Chem. Mater.* **25**, 17-26 (2013).
- 563 (54) Alvarez, E. *et al.* The structure of the aluminum fumarate metal-organic framework A520,
564 *Angew. Chem. Int. Ed.* **54**, 3664 -3668 (2015).
- 565 (55) Reinsch, H. *et al.* A new aluminium-based microporous metal-organic framework:
566 Al(BTB) (BTB = 1,3,5-benzenetrisbenzoate), *Micro. Meso. Mater.* **157**, 50-55 (2012).

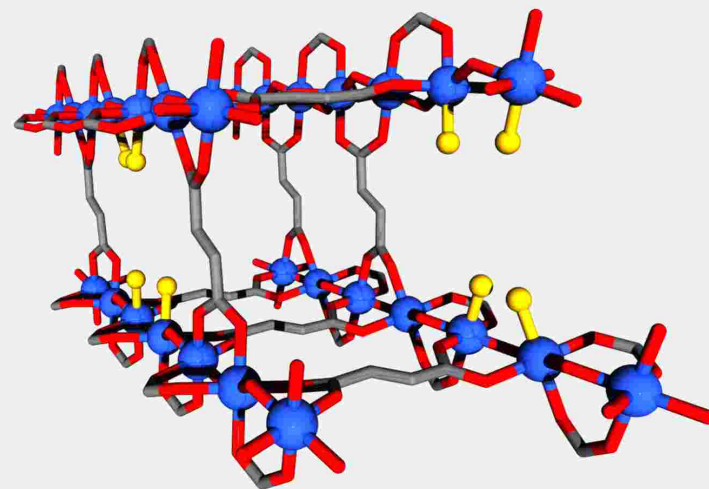
- 567 (56) Volkringer, C. *et al.* Occurrence of Uncommon Infinite Chains Consisting of Edge-Sharing
568 Octahedra in a Porous Metal Organic Framework-Type Aluminum Pyromellitate
569 $\text{Al}_4(\text{OH})_8[\text{C}_{10}\text{O}_8\text{H}_2]$ (MIL-120): Synthesis, Structure, and Gas Sorption Properties. *Chem.*
570 *Mater.* **21**, 5783 (2009).
- 571 (57) Volkringer, C. *et al.* Structural Transitions and Flexibility during Dehydration-Rehydration
572 Process in the MOF-type Aluminum Pyromellitate $\text{Al}_2(\text{OH})_2[\text{C}_{10}\text{O}_8\text{H}_2]$ (MIL-118). *Cryst.*
573 *Growth Des.* **9**, 2927 (2009).
- 574 (58) Krüger, M. *et al.* $[\text{Al}_2(\text{OH})_2(\text{TCPB})]$ – An Al-MOF based on a tetratopic linker molecule.
575 *Micro. Meso. Mater.* **216**, 27e35 (2015).
- 576 (59) Boyd, P. G. *et al.* Data-driven design of metal-organic frameworks for wet flue gas CO_2
577 capture. *Nature* **576**, 253-256 (2019).
- 578 (60) Yang, S. *et al.* Selectivity and direct visualization of carbon dioxide and sulfur dioxide in
579 a decorated porous host. *Nat. Chem.* **4**, 887-894 (2012).
- 580 (61) Huang, Z., Svensson, E., Jian, G., KenInge, L. & Zou, X. 3D electron diffraction as an
581 important technique for structure elucidation of metal-organic frameworks and covalent
582 organic frameworks. *Coord. Chem. Rev.* **427**, 213583 (2021).
- 583 (62) Gemmi, M. *et al.* 3D Electron Diffraction: The Nanocrystallography Revolution. *ACS*
584 *Cent. Sci.* **5**, 1315-1329 (2019).
- 585 (63) Nederlof, I., Genderen, E. V., Li, Y.-W. & Abrahams, J. P. A Medipix quantum area
586 detector allows rotation electron diffraction data collection from submicrometre three-
587 dimensional protein crystals. *Acta Crystallogr. D Biol. Crystallogr.* **69**, 1223-1230 (2013).

- 588 (64) Teufel, J. *et al.* MFU-4 – A Metal-Organic Framework for Highly Effective H₂/D₂
589 Separation. *Adv. Mater.* **25**, 635-639 (2013).
- 590 (65) Wan, W. & Zou, X. *CrystDiff*. DOI 10.5281/zenodo.2545681 (2019).
591
- 592 (66) Benoit, V. *et al.* MIL-91(Ti), a small pore metal-organic framework which fulfils several
593 criteria: an upscaled green synthesis, excellent water stability, high CO₂ selectivity and fast
594 CO₂ transport. *J. Mater. Chem. A.* **4**, 1383-1389 (2016).
- 595 (67) Gelfand, B. S. & Shimizu, G. K. H. Parameterizing and grading hydrolytic stability in
596 metal-organic frameworks. *Dalton Trans.* **45**, 3668-3678 (2016).
- 597 (68) Altomare, A. *et al.* EXPO2013: a kit of tools for phasing crystal structures from powder
598 data. *J. Appl. Cryst.* **46**, 1231-1235 (2013).
- 599 (69) Rodriguez-Carvajal, J. Recent advances in magnetic structure determination neutron
600 powder diffraction. *Physica B*, **192**, 55-69 (1993).
- 601 (70) Roslova, M. *et al.* InsteaDMatic: towards cross-platform automated continuous rotation
602 electron diffraction. *J. Appl. Crystallogr.* **53**, 1217-1224 (2020).
- 603 (71) Palatinus, L. *et al.* Specifics of the data processing of precession electron diffraction
604 tomography data and their implementation in the program PETS2.0. *Acta Crystallogr. Sect. B*
605 **75**, 512-522 (2019).
- 606 (72) Palatinus, L. & Chapuis, G. SUPERFLIP – a computer program for the solution of crystal
607 structures by charge flipping in arbitrary dimensions. *J. Appl. Crystallogr.* **40**, 786-790 (2007).

- 608 (73) Petříček, V. Dušek, M. & Palatinus, L. Crystallographic Computing System JANA2006:
609 General features. *Zeitschrift für Krist. - Cryst. Mater.* **229**, 345 (2014).
- 610 (74) Momma, K. & Izumi, F. VESTA 3 for three-dimensional visualization of crystal,
611 volumetric and morphology data. *J. Appl. Crystallogr.* **44**, 1272-1276 (2011).

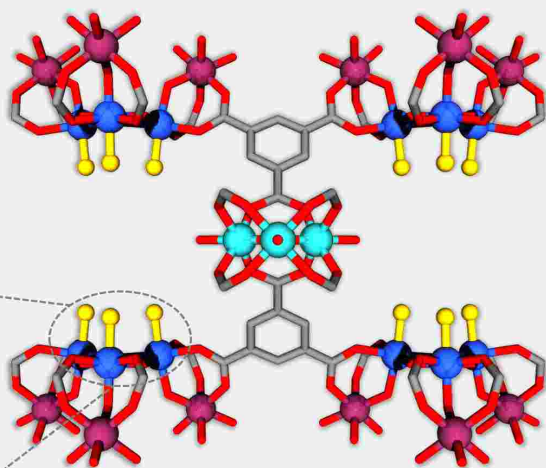


Missing linker defects in MIL-53(AI)-FA



Topological defective Al-MOFs

MIL-96(AI)



Al^{3+}

Towards topological defective Al-MOF

